Ultraviolet Oscillations in the Chromosphere of the Quiet Sun

R. T. James M^{c}Ateer[1]

j.mcateer@qub.ac.uk

Peter T. Gallagher[2,1]

Peter.T.Gallagher@gsfc.nasa.gov

D. Shaun Bloomfield[1]

s.bloomfield@qub.ac.uk

David R. Williams[3,1]

drw@mssl.ucl.ac.uk

Mihalis Mathioudakis[1]

m.mathioudakis@qub.ac.uk

Francis P. Keenan[1]

f.keenan@qub.ac.uk

[1]Department of Pure and Applied Physics, Queen's University Belfast, Belfast, BT7 1NN, Northern Ireland, U.K.

[2]L-3 Communications GSI, NASA Goddard Space Flight Center, Greenbelt, Maryland 20771, U.S.A.

[3]Mullard Space Science Laboratory, Holmbury St. Mary, Dorking, Surrey, RH5 6NT, U.K.

ABSTRACT

Quiet-Sun oscillations in the four *TRACE* ultraviolet passbands centred on 1700 Å, 1600 Å, 1216 Å and 1550 Å are studied using a wavelet-based technique. Both network and internetwork regions show oscillations with a variety of periods and lifetimes in all passbands. The most frequent network oscillation has a period of 283 s with a lifetime of 2–3 cycles in all passbands. These oscillations are discussed in terms of upwardly-propagating magnetohydrodynamic wave models. The most frequent internetwork oscillation has a period of 252 s, again with a lifetime of 2–3 cycles, in all passbands. The tendency for these oscillations to recur in the same position is discussed in terms of 'persistent flashers'. The network contains greater oscillatory power than the internetwork at periods longer than 300 s in the low chromosphere. This value is shown to decrease to 250 s in the high chromosphere. The internetwork also displays a larger number of short-lifetime, long-period oscillations than the network, especially in the low chromosphere. Both network and internetwork regions contain a small number of non-recurring long-lifetime oscillations.

Subject headings: Sun: oscillations – Sun: chromosphere – Sun: photosphere – Sun: UV radiation – methods: statistical

1. INTRODUCTION

The subject of chromospheric heating is one of the most studied and yet poorly understood areas of solar physics. A temperature minimum at ∼500 km above the photosphere, and the subsequent reversal of the temperature profile, suggests some unknown heating mechanism must be present to balance the energy lost by radiation. As this mechanism

cannot be due to either conduction or radiation (Narain & Agarwal 1994), chromospheric heating theories have mainly concentrated on heating via the dissipation of energy carried by waves. The mode of these waves, whether standing or travelling, the dominant restoring force (magnetic, gas pressure, gravity, etc.), and the resulting oscillations of the chromospheric plasma have been the subject of much deliberation (see reviews by Rutten & Uitenbroek 1991; Rutten 1999).

In the chromosphere, the quiet Sun displays a distinct network appearance identical to the supergranular cell structure in Dopplergrams (Leighton, Noyes, & Simon 1962). The nature of supergranular flow results in magnetic flux coalescing at cell vertices, with replenishment of flux occurring on the scale of a few days to a week (Schrijver et al. 1998). This creates a dense collection of flux tubes (Berger et al. 1998; Lites, Rutten, & Berger 1999) at these vertices and is observable as kilogauss fields in magnetograms. In time-integrated images of the chromosphere, the network is only partially defined as patches of increased intensity (network bright points), which display a one-to-one spatial correlation with this underlying photospheric magnetic field (Cauzzi, Falchi, & Falciani 2000; McAteer et al. 2003). On the other hand, the internetwork is mainly field-free, and appears dark on time-integrated images of the chromosphere.

This spatial dichotomy between the network and internetwork is also apparent in the Fourier spectrum of lightcurves from these two regions, leading to the suggestion that different heating mechanisms may dominate in each region (Gallagher et al. 1999). The internetwork contains oscillations with periodicities around 180 s (a broad 3–8 mHz peak in the Fourier spectrum: the acoustic band), intermittently present in small grains, and with a good correlation between the photosphere and the chromosphere (Lites, Rutten, & Kalkofen 1993). Some work shows the existence of nodal planes and hence standing waves (e.g., Kneer & von Uexküll 1993; Deubner, Waldschik, & Steffens 1996). Other studies show a directly

proportional increase of phase lag with frequency between lines formed at different heights in the atmosphere (e.g., Judge, Tarbell, & Wilhelm 2001; Wikstøl et al. 2000). This suggests the presence of upwardly-propagating acoustic waves, which have been successfully modelled by Carlsson & Stein (1992, 1997). Brandt et al. (1992) suggest a scenario whereby there are two types of grains: one with a long term memory, termed 'persistent flashers', with a magnetic dependence; and a second, 5–10 times more common, with no spatial memory or magnetic dependence. This may explain the difference between the conclusions reached by Worden, Harvey, & Shine (1999) and Lites et al. (1999), who suggest no correlation between the small internetwork magnetic fields and the chromospheric grains, and those of Sivaraman et al. (2000) who found a strong correlation between the internetwork grains and magnetic fields.

Longer-period network oscillations (5–20 mins) have not benefited from similarly detailed simulations, mainly due to the difficulty of modelling the chromospheric plasma in the presence of the kilogauss magnetic fields (Bogdan et al. 2003). Current theories of network heating suggest that the magnetic field is critical and these fall into three main categories: (i) *in situ* resistive dissipation from the stochastic rearrangement of magnetic field lines (Kneer & von Uexküll 1985, 1986); (ii) upwardly-propagating transverse magnetohydrodynamic (MHD) waves coupling, and hence transferring power, to longitudinal waves, which can then form shocks (Kalkofen 1997; Hasan & Kalkofen 1999; Hasan et al. 2003); (iii) resistive dissipation of Pedersen currents, driven by longitudinal MHD waves (Goodman 2000). Observations show a poor temporal correlation between chromospheric network oscillations and those in the underlying photosphere (Lites et al. 1993). Wavelet-based studies (Bocchialini & Baudin 1995; Baudin, Bocchialini, & Koutchmy 1996; McAteer et al. 2003; Bloomfield et al. 2003) show the existence of mainly upwardly-propagating (but also some downwardly-propagating) waves in the chromosphere at speeds close to the sound speed. Furthermore, the tendency of oscillations to occur in the very centre of network elements

(McAteer et al. 2002), combined with a lack of both intensity and oscillatory power near, but not directly above, photospheric network elements (termed 'magnetic shadows'), suggests the existence of mode-conversion of acoustic waves as they interact with the magnetic canopy (Judge et al. 2001; McIntosh & Judge 2001; McIntosh, Fleck, & Judge 2003).

We present an automated wavelet analysis approach (originally applied to CDS data by Ireland et al. 1999) to *Transition Region and Coronal Explorer* (*TRACE*; Handy et al. 1998a) quiet-Sun ultraviolet (UV) oscillations for both the network and internetwork, and discuss the results in each region in relation to the above heating mechanisms. When studying quiet-Sun data, wavelet analysis has two specific benefits over the Fourier transform. Firstly, the intermittency of the oscillations present (Banerjee et al. 2001; Hansteen, Betta, & Carlsson 2000) means that their Fourier power may be swamped by the much longer non-periodic component, whereas wavelet analysis provides localised temporal information. Secondly, quiet-Sun datasets are difficult to align compared to active region datasets due to a relative lack of features. Again the time-localised nature of wavelet analysis is better suited than Fourier analysis in dealing with frames which may not be perfectly aligned (Ireland et al. 1999). In order to reduce alignment problems, *TRACE* was used to provide long duration observations of the Sun, free of atmospheric distortions. The large field of view (FOV) of *TRACE* makes it very useful for quiet-Sun studies, where it provides a larger spatial sample than slit-based spectrometers (e.g., SUMER, CDS). The large passbands of *TRACE* also mean that any oscillations present are free from Doppler-shift effects due to plasma motions. Oscillations must therefore be due to changes in temperature and/or density. However, it is noted that the wide passbands make it difficult to estimate their height of formation (HOF), as each passband contains significant contributions from continuum in addition to line emission. The wide passbands may also lead to phase averaging.

The outline of this paper is as follows. An overview of the dataset, including a discussion

of the HOF of each passband, is presented in Section 2. The alignment procedure, creation of the network/internetwork subsets and high-pass filtering are discussed in Section 3. This is followed by a detailed description of the wavelet analysis routine designed to search for both periodicity and lifetime of any oscillations in all the pixels in each subset. Section 4 compares the differing results from the network and internetwork, while our conclusions are given in Section 5.

2. OBSERVATIONS

A dataset from 1999 May 4 containing quiet-Sun images in the four UV passbands (1700 Å, 1600 Å, 1216 Å, 1550 Å) with a FOV of $128'' \times 320''$ was selected for this study. Further details of the dataset can be found in Krijger et al. (2003). A simple investigation into the frame rate stability in each passband resulted in a constant cadence of 40.05 s being assumed for the purpose of both Fourier and wavelet analyses. After image 168 there was a 50 s delay, corresponding to a small change in the FOV as *TRACE* compensated for solar rotation. For this reason the data were divided into two equal timeblocks; block A containing images 1–168 and block B containing images 169–336. This creation of two data blocks was also vital for data analysis (Sections 3.1 and 3.2) and to the search for oscillation recurrence (Section 4.3). In some cases there were 80 s time gaps between images. It was assumed this was due to a missing image. These missing images were replaced by an average of the (aligned) preceding and following images. Any images severely contaminated by cosmic rays were cleaned using programs available in the *TRACE* branch of the SolarSoftWare (SSW; Freeland & Handy 1998) tree of IDL.

2.1. Heights of Formation

Their are well-know difficulties associated with attributing HOFs to emission from broadband filters. Due to the complexity of line emission and continuum, any HOF will vary in both time (e.g., during a flare) and space (e.g., plage/network – internetwork). Whilst realising the limitations of any assigned HOF we suggest the following. Previous work with *TRACE* UV data (Judge et al. 2001; Krijger et al. 2001; Handy et al. 1998a) place the 1700 Å band lowest in the atmosphere (UV continuum at $\sim$4–10$\times10^3$K, below temperature minimum), followed by the 1600 Å passband (UV continuum at $\sim$4-10$\times10^3$K plus Fe II at $\sim$1.3$\times10^4$K, temperature minimum). Up to 50% of the signal in the 1216 Å passband is also believed to be UV continuum (Worden et al. 1999) suggesting a HOF around the mid chromosphere (50% Ly α at $\sim$1-3$\times10^4$K, plus 50% UV continuum). The 1550 Å passband has the highest HOF, at $\sim1\times10^5$K, but with sigificant contributions from other lines (e.g., Si II at $\sim1\times10^4$K) and continuum. These temperatures are approximate and there is expected to be a degree of overlapping emission between passbands. However in order to carry out a qualitative discussion of our results, we assume a sequence of increasing HOF of 1700 Å, 1600 Å, 1216 Å, 1550 Å.

Techniques have been developed to separate both the Ly α (Handy et al. 1999) and C IV (Handy et al. 1998b) emission from the continuum. However in both cases it is shown that these techniques are only reliable for more intense solar features (e.g., Figure 6 of Handy et al. 1999). The bright network will be at the lower limit of this intensity, and the techniques are certainly not applicable to the internetwork without long exposure times. As we wish to compare network and internetwork oscillations we decided not to apply any continuum removal to the data.

3. DATA ANALYSIS

3.1. Alignment

The division of the data into two blocks was vital to compensate for solar differential rotation in the dataset (estimated as $1''$ over each 167 image block). Initially all wavelengths were aligned by calculating the offsets of the middle image of each block to the corresponding 1600 Å image, and shifting all images in each wavelength correspondingly. At each wavelength, all images were then aligned to the middle image of the timeseries using cross-correlation programs available in SSW. Any large offsets were replaced by the average of the preceding and following offsets, and the cross-correlation repeated until all offsets were less than 0.2 pixels (i.e., $0.1''$). This procedure was carried out for each block separately. Finally, the offset of the middle image of block A to block B was found using the same cross-correlation procedure and all block B data were shifted by this offset. This resulted in the entire timeseries, in all four UV wavelengths being aligned to within $0.1''$. Due to solar rotation, several pixel rows and columns were not always present in the data, so that the aligned data FOV was reduced from 256×640 pixels^2 to 215×600 pixels^2.

3.2. Creation of Network and Internetwork Subsets

The nature of the network to appear bright in time-averaged images is used to define a network/internetwork mask in a method similar to Krijger et al. (2001). For the aligned 1600 Å data, a time-averaged image was created for each block. For each time-averaged image, a histogram of pixel values was created. Pixels with an intensity below the modal intensity value were defined as internetwork, while those with an intensity value greater than one standard deviation above the mean intensity value were defined as network (McAteer et al. 2002; Worden et al. 1999). The subsequent network pixel arrays for block A and block

B were compared, and only pixels defined as network in both datablocks were retained. A similar process was carried out for the internetwork. The resulting network and internetwork pixels are displayed in Figure 1. The leftmost image is the time-averaged 1600 Å block A, where the network appears as bright clusters at supergranular cell vertices. The network and internetwork pixels are contoured in the rightmost image, according to the masks in the middle image (where white is the network mask and black is internetwork mask). These masks were then applied to all four UV passbands.

3.3. Filtering

With 167 images at 40.05 s cadence, the Nyquist frequency is 11.1 mHz and the frequency resolution is 0.13 mHz. After subtracting the mean this provides a range of detectable periodicity of 90–7692 s. A high-pass filter was employed such that all Fourier power below ∼0.6 mHz (above ∼1642 s in period space, corresponding to the maximum possible detectable period, see Section 3.4, Equation 3 and Figure 2) was removed. The importance of filtering is to increase the significance of the expected peak around 3–5 min by reducing aliasing effects. Filtering was carried out on each lightcurve by convolution with a suitable Bessel function so as to provide a smooth edge to the filter profile, and hence reduce ringing effects.

3.4. Wavelet Analysis

A wavelet analysis was carried out on each lightcurve using a Morlet wavelet of the form

$$\psi(\eta) = \pi^{-1/4} \exp(i\omega_0 \eta) \exp\left(\frac{-\eta^2}{2}\right) \ , \tag{1}$$

where $\eta = t/s$ is the dimensionless time parameter, t is the time, s is the scale of the wavelet, $\omega_0 = s\omega$ is the dimensionless frequency parameter (ω_0=6, to satisfy the admissibility condition; Farge 1992), and $\pi^{-1/4}$ is a normalisation term. For the Morlet wavelet, the Fourier

period is ∼1.03 times the wavelet scale (Torrence & Compo 1998). At each point in time this provides a real and imaginary part to the wavelet transform. The wavelet power transform is then the square of the absolute value of the wavelet transform. A typical wavelet power transform for a network lightcurve is shown in Figure 2. Here the abscissa is time, t, and the ordinate is period, P. This is displayed on a linear intensity scale, such that brighter areas correspond to greater oscillatory power. The contours are at the 95% significance level and the two slanted lines define the cone-of-influence (COI). Edge effects are significant above these two lines. The extent of the COI, from the beginning and the end of the time series, at each period P, is defined in Torrence & Compo (1998) for the Morlet wavelet, as the decorrelation time for a spike in the time series, $t_d = \sqrt{2}P/1.03$ s . For example, for the dashed lines on Figure 2 at P=1200 s, the COI extends from t=0–1647 s, and from t=5001–6648 s. After creating the wavelet power transform, an automated routine calculated the lifetime and periodicity of any oscillations following the procedure first described in Ireland et al. (1999). First, all power below the 95% significance level or above the COI lines was removed. The routine then searches for any remaining power maxima. The lifetime of the oscillation at the period of each power maximum is defined as the interval of time from when the power reaches above 95% significance to when it dips below 95% significance again. The lifetime was then divided by the period to give a lifetime in terms of complete cycles. For example, for the oscillatory power in contour A in Figure 2, the lifetime is given by (4900-3500)/300 = 4.67 cycles. Any oscillations lasting for less than t_d (e.g., for the maxima in contour C in Figure 2, lifetime = (5100-4400)/650=1.08 cycles) were discarded as possibly being due to a spike in the time series. From the criterion of a lifetime of at least $\sqrt{2}P/1.03$ outside the COI (of size $2\sqrt{2}P/1.03$), the maximum possible detectable period, P_{max} can be obtained from

$$\frac{3\sqrt{2}\ \mathrm{P}_{max}}{1.03} = \delta \mathrm{t} \times (\mathrm{N} - 1), \tag{2}$$

where δt is the cadence, and N is the number of data points in the lightcurve (hence $\delta t \times (N-1)$ is the total duration of the lightcurve). Rearranging,

$$P_{max} = \frac{1.03 \times 40.05 \times 167}{3\sqrt{2}} = 1642 \text{ s.} \quad (3)$$

P_{max} is shown as the dash–dot line in Figure 2, and is the value used as the cut-off for the high pass filter (Section 3.3). The final output from the routine is a list of lifetimes and periodicities for all oscillations in each input lightcurve.

4. RESULTS AND DISCUSSION

4.1. Internetwork Oscillations

A summary of all internetwork oscillations for the first half (block A) of the 1700 Å data is shown in Figure 3. Here the ordinate is the period, P, as determined from the wavelet analysis. The nature of wavelet analysis means that the values of period increase logarithmically. The abscissa, l, is the oscillation lifetime binned to integer values. For example, the lifetime of 4.67 cycles discussed above is placed in the 4–5 bin. The horizontal dashed line is at $\sqrt{2}/1.03$ cycles (minimum lifetime), the vertical dashed line is at the Nyquist frequency, while the two solid vertical lines are at 3 and 5 min. The curved dashed line refers to the maximum number of complete cycles which can be observed at each period (due to the finite length of the time series). Figure 3 is plotted on a inverted linear intensity scale, such that darker areas correspond to a larger number of pixels with oscillations at period P, for lifetime l. The four colour bands refer to the upper quartile (black; $> 75\%$ of peak value), mid-upper quartile (dark grey; 50–75% of peak value), mid-lower quartile (light grey; 25–50% of peak value) and lower quartile (lightest grey; $< 25\%$ of peak value). The data have been divided by the number of pixels (hence number of lightcurves), to make all results from the network and internetwork directly comparable.

Figure 3 displays several interesting features. The most common oscillation is a well defined peak with a period of $\log_{10}(P)$=2.33 ($P\sim$210 s), lasting for 2–3 cycles, with an occurrence rate of 0.26 (i.e., 1 in 4 pixels contain an oscillation at this period for this lifetime). There are few oscillations below $\log_{10}(P)$=2.2 ($P\sim$160 s), and all the long-lifetime oscillations (LLOs; defined as >8 cycles) occur near the acoustic band (i.e., $\log_{10}(P)\sim$2.2–2.5). The internetwork results from the other UV passbands display a similar behaviour.

By summing Figure 3 over the lifetime axis we can create occurrence rate curves which are directly comparable to the average Fourier power curves (Figure 4). These occurrence rate curves have also been divided by a probability correction curve, to account for the fact that short-period oscillations are more likely to be observed (less time to undergo $\sqrt{2}/1.03$ cycles, and more lightcurve outside the COI). In Figure 4 the ordinate is the occurrence per pixel (i.e., average number of cycles) for the top panel, and average Fourier power per pixel for the bottom panel. Both panels share the same abscissa as Figure 3, namely period on a log scale. Again the two vertical lines are at 3 and 5 min. A simple Gaussian fit (i.e., with no continuum) has been applied to the feature around the acoustic band and overplotted in each case. The Gaussian fit was applied to the region of the curve from where it rises above zero, to the minimum around $\log_{10}(P)$=2.6. The value of the centre of the Gaussian fit (COG), and one sigma width are displayed in the top right corner of each plot. It should be noted that this width is an indication of the spread of frequencies around the peak. The estimated error in the determination of the position of the centre of the Gaussian is typically around 0.005 in $\log_{10}(P)$ (i.e., $\delta P\sim$4 s), and hence much smaller than the one sigma width.

Figure 4 shows the good agreement between the wavelet analysis and classical Fourier approach. It displays a rise of power (Fourier) and occurrence rate (wavelet) with increasing period, reaching a maximum around $\log_{10}(P)$=2.4 ($P\sim$250 s). This value differs from the peak in Figure 3 because of the probability correction curve applied to the data. Both curves

reach a minimum around $\log_{10}(P)$=2.6 (P∼400 s), followed by a gradual increase at higher periods. Using phase analysis techniques, Krijger et al (2001) attribute this high period power primarily to internal gravity waves, with some contribution from granular overshoot and the low-frequency tail of acoustic interference. The fall-off at $\log_{10}(P)$ >3.0 is due to the high-pass filter applied to the lightcurves.

4.2. Network Oscillations

A summary of all network pixel oscillations from the first half of the 1700 Å data is displayed in Figure 5. In contrast to the results from the internetwork pixels, the most common network oscillation is a well defined peak with a longer period of $\log_{10}(P)$=2.41 (P∼260 s), lasting for 2–3 cycles, with a lower occurrence rate of 0.19 (i.e., 1 in 5 pixels contain an oscillation at this period for this lifetime; the distribution of the occurrence rate is broader in the network). As in the internetwork, there are few oscillations below $\log_{10}(P)$=2.2 (P∼160 s), and all the LLOs occur near the acoustic band. However, the network contains an extended tail at the 25–50% level up to periods of $\log_{10}(P)$=2.9 (P∼800 s). Hasan & Kalkofen (1999) suggest a scenario whereby kink-mode waves generated in the photospheric network may travel up through the chromosphere, before coupling with saugage-mode waves. The extended tail of the network oscillations in Figure 5 may be the oscillatory signature of the kink-mode wave at P=534 s ($\log_{10}(P)$=2.73). In the 1216 Å and 1550 Å passbands this tail is less evident, hence these waves may have coupled in the high chromosphere.

Figure 6 repeats the comparison of the wavelet analysis and classical Fourier approaches of Figure 4, but applied to the network data. Figure 6 displays a rise of power (Fourier) and occurrence rate (wavelet) with increasing period, reaching a maximum around $\log_{10}(P)$=2.45 (P∼280 s). The two curves reach a minimum around $\log_{10}(P)$=2.6 (P∼400 s), followed by a gradual increase. Again the fall-off at $\log_{10}(P)$ >3.0 is due to the high-pass filter performed

on the lightcurves.

4.3. Oscillation Recurrence

By comparing how many pixels in block A of each wavelength display a similar behaviour in block B, it is possible to study whether oscillations of specific period and lifetime occur repeatedly. At each wavelength all network pixels displaying periodicity between 230–280 s in block A were selected and compared to network pixels containing periodicity in the same range in block B. This showed a recurrence rate of ∼65–75% in all four UV passbands. This was also carried out for all network pixels displaying oscillations lasting 2–3 cycles at all periods (where the corresponding value was ∼75-85%). A study of all network pixels lasting 2–3 cycles *and* in the range 230–280 s (i.e., at the peak value in the lifetime-period plots), showed ∼40% common pixels. As these oscillations are the most frequent, a 40% chance of a recurrence at the same position represents a good candidate for repeated heating of the surrounding plasma.

In the internetwork, the fraction of pixels showing oscillations recurring in the same location was generally 5–10% higher than in the network. The internetwork oscillations lasting 2–3 cycles *and* in the range 230–280 s (with a ∼50% recurrence rate) may be the persistent flashers first identified by Brandt et al. (1992). However their studies suggest grains which are persistent flashers should be 5-10 times less likely to occur than normal K_{2V} grains, which in turn suggests a recurrence rate of ∼10–17%. The higher value of 50% obtained in these data could be due to the internetwork mask preferentially containing persistent flashers rather than normal internetwork grains.

4.4. Long-Lifetime Oscillations

During each cycle, a wave may transfer a portion of its energy to the surroundings. Hence, any long-lifetime oscillations, which undergo several complete cycles, are good candidates for chromospheric heating. In all the UV passbands, in both the network and internetwork, all the LLOs occur near the acoustic band. At longer periods, oscillations tend to last for fewer cycles, and are even more transient at shorter periods. These LLOs never recur in the same place in both blocks of the data. This suggests that the source, in driving the LLO, no longer has sufficient energy to create further oscillations (or if it does create further oscillations, they will be too weak or have short lifetimes, hence will not be detected). Of course it may be that LLOs do recur, but more than 111 minutes (167×45 s) apart. It is also noted that the lower HOF passbands (1700 Å,1600 Å) contain more LLOs than the upper passbands, and whereas 1.5–2.0% of network pixels contains LLOs, only 0.05% of internetwork pixels display LLOs. Further studies of more LLOs are necessary to confirm these effects.

4.5. Network - Internetwork Comparison

From a comparison of the network and internetwork results in all passbands, a few common themes are apparent. As often confirmed before, the network tends to oscillate with a period close to 5 min. The internetwork, whilst exhibiting many more oscillations around 3 min, contains a peak close to 4 min. Table 1 contains a list of the centre of the Gaussian fits and one sigma widths for the Fourier and wavelet approaches. The calculated averages of the COGs for the Fourier and wavelet approaches agree within the one sigma widths and both regions contain a wide range of periodicities. The widths are typically larger in the Fourier than the wavelet approach, but in both cases a range of $\sim \log_{10}(P)$=2.1–2.6 is fitted (2.5–7.9 mHz; other work (e.g. Lites et al. 1999; McIntosh et al. 2003) sums over

3–8mHz). This periodicity range is important to remember when using the 3- and 5-min oscillations in modelling.

The power of the dominant oscillations in each region was studied using several different methods. Table 2 contains a summary of the occurrence rate of the peak periodicity in both the lifetime-period diagrams (e.g., Figures 3 and 5) and the centre of the Gaussian fits to the average occurrence rate and Fourier power diagrams (e.g., Figures 4 and 6) in all passbands. It is immediately apparent that the results from the second half of the 1550 Å dataset (1550 B) display very low values in both the network and internetwork. These low values may be due to the larger number of saturated pixels, dropped data and streaks in this part of the dataset. Hence for the following interpretation, the 1550 B dataset is ignored.

For the network, the lifetime-period approach (column 2) shows an increasing occurrence rate with increasing HOF from 1700 Å through 1600 Å to 1216 Å. It then decreases in 1550 Å. This trend is also prevalent in the values of the COG fit for the occurrence rate (column 4) and the COG fit for the Fourier power of data block B (bottom of column 6), suggesting oscillations occurring more frequently, leading to an increase in oscillatory power, as waves move up through the atmosphere to the HOF of the 1216 Å passband. As the number, as well as the total oscillatory power, increases, this suggests that waves are exciting oscillations in neighbouring regions as they propagate through the atmosphere. Before the waves reach the 1550 Å passband HOF several of these oscillations are no longer observed. There are a number of possible explanations for this decrease in both occurrence and power of oscillations: (i) waves may either shock or damp between the HOF of 1216 Å and 1550 Å; (ii) at the height where the canopy closes over completely, the magnetic field lines may be almost horizontal, and hence may channel oscillations away from areas defined as network; (iii) upwardly-propagating acoustic waves near network areas may undergo mode-conversion when interacting with the closing magnetic canopy in the upper chromosphere (Judge et al.

2001), hence oscillations will change in frequency. It is difficult to determine which one, or combination of two or more, of these explanations is correct.

From a comparison of the Fourier and wavelet approaches in Table 2 it is clear that the internetwork normally has a higher value of oscillatory power (Fourier) and occurrence rate (wavelet) than the network. For the lifetime-period approach (column 3), the occurrence rate decreases from the 1700 Å HOF to the 1600 Å HOF, then increases at the 1216 Å HOF, and decreases again at the 1550 Å HOF. This trend is repeated in the COG fitting approach (column 5, column 7 bottom). Therefore some waves at the 1700 Å HOF must disappear before the 1600 Å HOF. This agrees with the low-lying shocks in internetwork grain simulations of Carlsson & Stein (1992, 1995). Above the 1600 Å HOF both long- and short-period waves will produce shocks separated by the acoustic cut-off period (Carlsson & Stein 1992), which may explain the increase at 1216 Å. The subsequent decrease at the 1550 Å HOF may then be due to a decreased number of these oscillations propagating to this height.

4.6. Network - Internetwork Dominance

Krijger et al. (2001) show that the network oscillatory power exceeds that in the internetwork for all frequencies below ∼5 mHz (their Figure 12). The time-localised nature of wavelet analysis can be used to extend this type of study into the temporal domain. In each bandpass, an average network and internetwork lifetime-period diagram was created (i.e., an average of block A and block B, except in 1550 Å where only block A data was used - Section 4.5). A comparison diagram was then created by comparing the network occurrence rates to the internetwork occurrence rates at each period and lifetime. Figure 7 shows the resulting network / internetwork comparison for all datasets. In each column, the top part has the same axes and lines as Figure 3 (also Figure 5). Black parts of the top row of Figure 7

refer to where the network has a greater occurrence rate, whereas grey parts refer to where the internetwork dominates. The middle and bottom row of Figure 7 are directly comparable to Figures 4 and 6. In these plots, the solid line refers to network data, and a dashed line to internetwork. It is clear from the middle and bottom rows that the network has greater oscillatory power at all periods longer than $\log_{10}(P)$=2.45 (P∼280 s; 3.6 mHz). There is also a tendency for this cross-over period to decrease with increasing HOF (from ∼300 s in 1700 Å to ∼250 s in 1550 Å). However the top row in Figure 7 displays a further feature. If the network dominates for all lifetimes at periods above $\log_{10}(P)$=2.45, then the resulting plots in the top row should be entirely black to the right of this cross-over, and entirely grey to the left of this cross-over. Instead there are regions of internetwork domination above $\log_{10}(P)$=2.45 for a small number of cycles. This mixing is more prevalent in the 1700 Å and 1600 Å data than for the 1216 Å and 1550 Å, suggesting these short-lifetime, long-period internetwork oscillations are most likely a low-chromosphere phenomenon. There is also some mixing at short periods, which may be examined further by using a higher-cadence dataset.

5. CONCLUSIONS

A new automated wavelet analysis approach (based on an original idea in Ireland et al. 1999) to *TRACE* quiet-Sun UV data is presented. This permits the extension of previous Fourier analysis into the time-localised domain. The resulting occurrence rate at specific periods and lifetimes is directly comparable to the results of the classical Fourier approach. The network is found to have a peak occurrence rate periodicity of $\log_{10}(P)$=2.451±0.087 (P=231–346 s) for a lifetime of 2–3 cycles, with a significant tail of higher-period oscillations, while the internetwork is found to have a well-defined peak occurrence rate periodicity of $\log_{10}(P)$=2.402±0.090 (P=205–309 s) for a lifetime of 2–3 cycles. Both the network and

internetwork show a number of long-lifetime oscillations, however these do not seem to recur in the same location. Consequently the driver may have exhausted its energy in generating the LLO. On the other hand, oscillations at 230–280 s, and/or 2–3 cycles, show a tendency to recur at the same spatial position. These are considered good candidates for chromospheric heating. Network oscillations show an increase in occurrence rate and oscillatory power with increasing HOF from 1700 Å to 1216 Å, possibly as a result of the opening up of the canopy at higher altitudes. In the 1550 Å passband there is a marked decrease in both occurrence rate and oscillatory power, suggesting that any possible waves may have either dissipated, shocked, moved away from the network or changed in frequency. The network also contains more oscillations around 534 s in the lower HOF than upper HOF passbands, which agrees with the MHD model of Hasan & Kalkofen (1999). In the internetwork there is a decrease in occurrence rate from 1700 Å to 1600 Å. Hence, some oscillations seem unable to propagate past the low chromosphere. However, the increase at 1216 Å and subsequent decrease at 1550 Å suggests that some waves which do propagate through the low-chromosphere may once again excite further oscillations, before disappearing higher in the atmosphere. A comparison of the occurrence rate of oscillations in the network and internetwork shows that although the network generally dominates at periods greater than 300 s, for a small number of cycles and long periods the internetwork may dominate. Similarly, regions of network dominance may be found at very short periods (and low lifetimes) where Fourier analysis shows internetwork oscillations to dominate.

A study into the spatial position of pixels displaying different periodicities and lifetimes may answer some of the questions posed in this paper. It may be useful to apply this method to higher-cadence *TRACE* quiet-Sun datasets and other instruments. It can also be extended into a third spatial region between the network and internetwork (classified as 'intermediate' in Krijger et al. 2001). In a wider context, this technique can be used in other areas of solar physics (e.g., active regions) or astronomy in general where a search

for transient, spatially-localised, oscillatory power is required (e.g., multi-target wide-field imaging).

This work was funded by a CAST award and PhD studentships from Queen's University Belfast and Department for Education and Learning (NI). FPK is grateful to AWE Aldermaston for the award of a William Penney Fellowship. JMA is thankful to J. Ireland and J. M. Krijger for helpful discussion regarding the wavelet routines and image segmentation. Wavelet software was provided by C. Torrence and G. Compo.[4]

[4]URL http://paos.colorado.edu/research/wavelets/

REFERENCES

Banerjee, D., O'Shea, E., Doyle, J. G., & Goossens, M. 2001, 371, 1137

Baudin, F., Bocchialini, K., & Koutchmy, S. 1996, A&A, 314, L9

Berger, T. E., Löfdahl, M. G., Shine, R. S.,& Title, A. M. 1998, ApJ, 495, 973

Bogdan, T. J., et al. 2003, ApJ, submitted

Bloomfield, D. S., McAteer, R. T. J., Mathioudakis, M., Williams, D. R., & Keenan, F. P. 2003, ApJ, submitted

Bocchialini, K., & Baudin, F. 1995, A&A, 299, 893

Brandt, P. N., Rutten, R. J., Shine, R. A., & Trujillo Bueno, T. 1992, in Cool Stars, Stellar Systems, and the Sun, Proc. 7th Cambridge Workshop, eds M. S. Gaimpapa & J. A. Bookbinder, 26, 121

Carlsson, M., & Stein, R. F. 1992, ApJ, 397, L59

Carlsson, M., & Stein, R. F. 1997, ApJ, 481, 500

Cauzzi, G., Falchi, A., & Falciani, R. 2000, A&A, 357, 1090

Deubner, F.-L., Waldschik,Th., & Steffens, S. 1996, A&A, 307, 936

Farge, M. 1992, Annu. Rev. Fluid Mechanics , 24, 395

Freeland, S. L., & Handy, B. N. 1998, Sol. Phys., 182, 497

Gallagher, P. T., Phillips, K. J. H., Harra-Murnion, L. K., Baudin, F., & Keenan, F. P. 1999, A&A, 348, 257

Goodman, L.M. 2000, ApJ, 533, 501

Handy, B.N., et al. 1998a, Sol. Phys., 187, 229

Handy, B. N., Bruner, M. E., Tarbell, T. D., Title, A. M., Wolfson, C. J., Laforge, M. J., & Oliver, J. J. 1998b, Sol. Phys., 183, 29

Handy, B. N., Tarbell, T. D., Wolfson, C. J., Korendyke, C. M., & Vourlidas, A. 1999, Sol. Phys., 190, 351

Hansteen, V. H., Betta, R., & Carlsson, M. 2000, A&A, 360, 742

Hasan, S. S., & Kalkofen, W. 1999, ApJ, 512, 899

Hasan, S. S., Kalkofen, W., van Ballegooijen, A. A., & Ulmschneider, P. 2003 , ApJ, 585, 1138

Ireland, J., Walsh, R. W., Harrison, R. A., & Priest, E. R. 1999, A&A, 347, 355

Judge, P. G., Tarbell, T. D., & Wilhelm, K. 2001, ApJ, 554, 424

Kalkofen, W. 1997, ApJ, 486, L145

Kneer F., & von Uexküll, M. 1985, A&A, 144, 443

Kneer F., & von Uexküll, M. 1986, A&A, 155, 178

Kneer F., & von Uexküll, M. 1993, A&A, 274, 584

Krijger, J. M., Rutten, R. J., Lites, B. W., Straus, Th., Shine, R. A., & Tarbell, T. D. 2001, A&A, 379, 1052

Krijger, J. M., Heinzel, P., Curdt, W., & Schmidt, W. 2003, A&A, sub

Leighton, R. B., Noyes, R. W., & Simon, G .W. 1962, ApJ, 135, 474

Lites, B. W., Rutten, R. J., & Berger, T. E. 1999, ApJ, 517, 1013

Lites, B. W., Rutten, R. J., & Kalkofen, W. 1993, ApJ, 414, 345

McAteer, R. T. J., Gallagher, P. T., Williams, D. R., Mathioudakis, M., Phillips, K. J. H., & Keenan, F. P. 2002, ApJ, 567, L165

McAteer, R. T. J., Gallagher, P. T., Williams, D. R., Mathioudakis, M., Bloomfield, D. S., Phillips, K. J. H., & Keenan, F. P. 2003, ApJ, 587, 806

McIntosh, W. S., & Judge, P. G. 2001, ApJ, 561, 420

McIntosh, W. S., Fleck, B., & Judge, P. G. 2003, A&A, 405, 769

Narain, U., & Agarwal, P. 1994, Bull. Astr. Soc. India, 22, 111

Rutten, R. J. 1999 in ASP Conf. Ser. 184, Proc. 3rd Adv. Solar Physics Euroconference, eds B. Schmieder, A. Hoffman, & J. Staude (San Francisco: ASP),181

Rutten, R. J., & Uitenbroek, H. 1991, Sol. Phys., 134, 15

Schrijver, C. J., et al. 1998, Nature, 394, 152

Sivaraman, K. R., Gupta, S. S., Livingston, W. C., Damé L., Kalkofen, W., Keller, C. U., Smartt, R., & Hasan, S. S. 2000, A&A, 363, 279

Torrence, C. & Compo, G. P. 1998, Bull. Amer. Meteor. Soc., 79, 61

Wikstøl, Ø., Hansteen, V. H., Carlsson, M., & Judge, P. G. 2000, ApJ, 531, 1150

Worden, J., Harvey, J., & Shine, R. 1999, ApJ, 523, 450

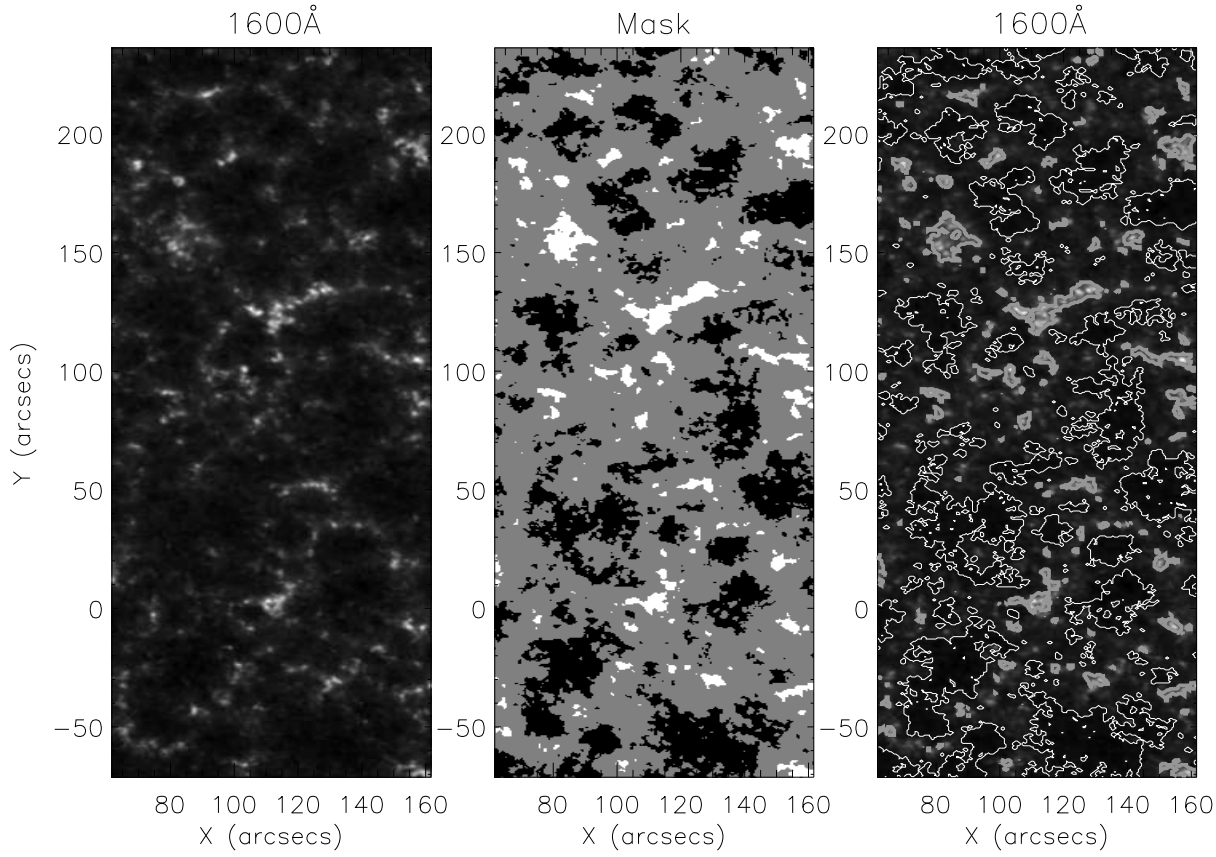

Fig. 1.— Left: Time averaged (data block A) 1600 Å image. Middle: The network (white) and internetwork (black) masks. Right: Network (bright) pixels are contoured with thick grey lines. Internetwork (dark) pixels are contoured with thin white lines.

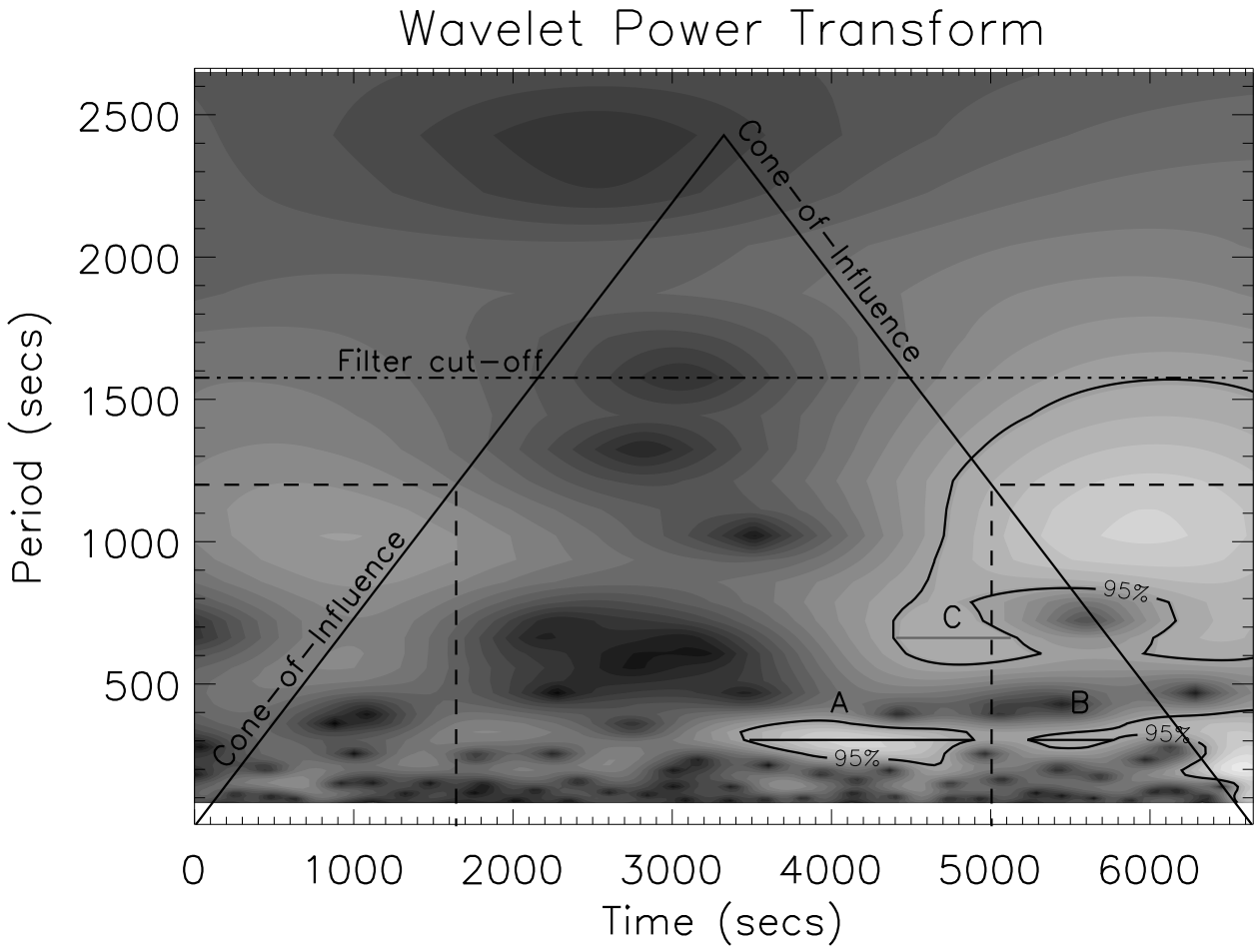

Fig. 2.— Wavelet power transform of a typical network lightcurve. The two slanted lines define the cone-of-influence, the size of which at a period of 1200 s is shown by the dashed lines as being 1647 s at each end of the time series. The dash-dot line is at 1624 s, the cut-off of the high-pass filter. The contours are at the 95% confidence level. The three maxima outside the cone-of-influence are marked A, B, and C, and the solid horizontal lines define their lifetimes.

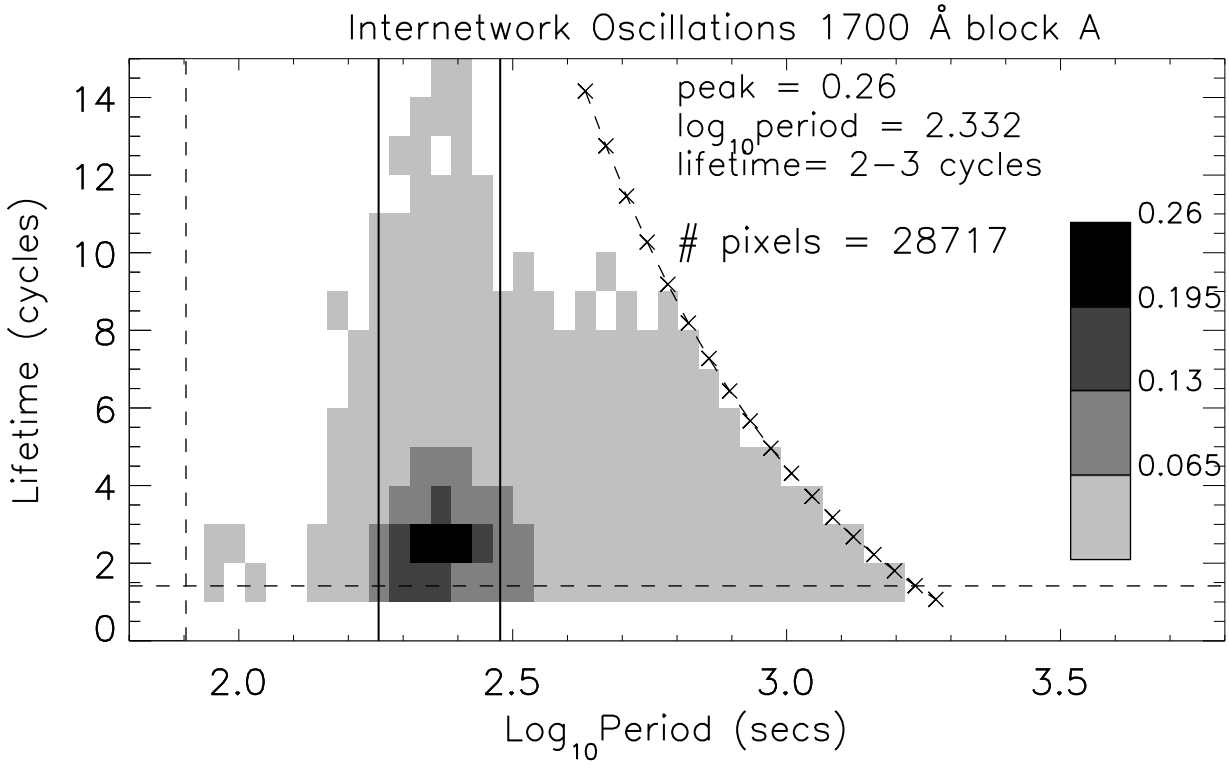

Fig. 3.— Summary of all internetwork oscillations for the 1700 Å block A dataset (28717 pixels). The frequency of occurrence of any oscillation at each period and lifetime is plotted according to the intensity scale on the right. The dashed vertical and horizontal lines are at the Nyquist frequency and minimum lifetime, respectively. The two solid vertical lines are at 3 and 5 min. The curved dashed line defines the maximum detectable number of cycles for each period. The four shades of grey corresponds to >75%, 50–75%, 25–50%, <25% of the maximum value (0.26).

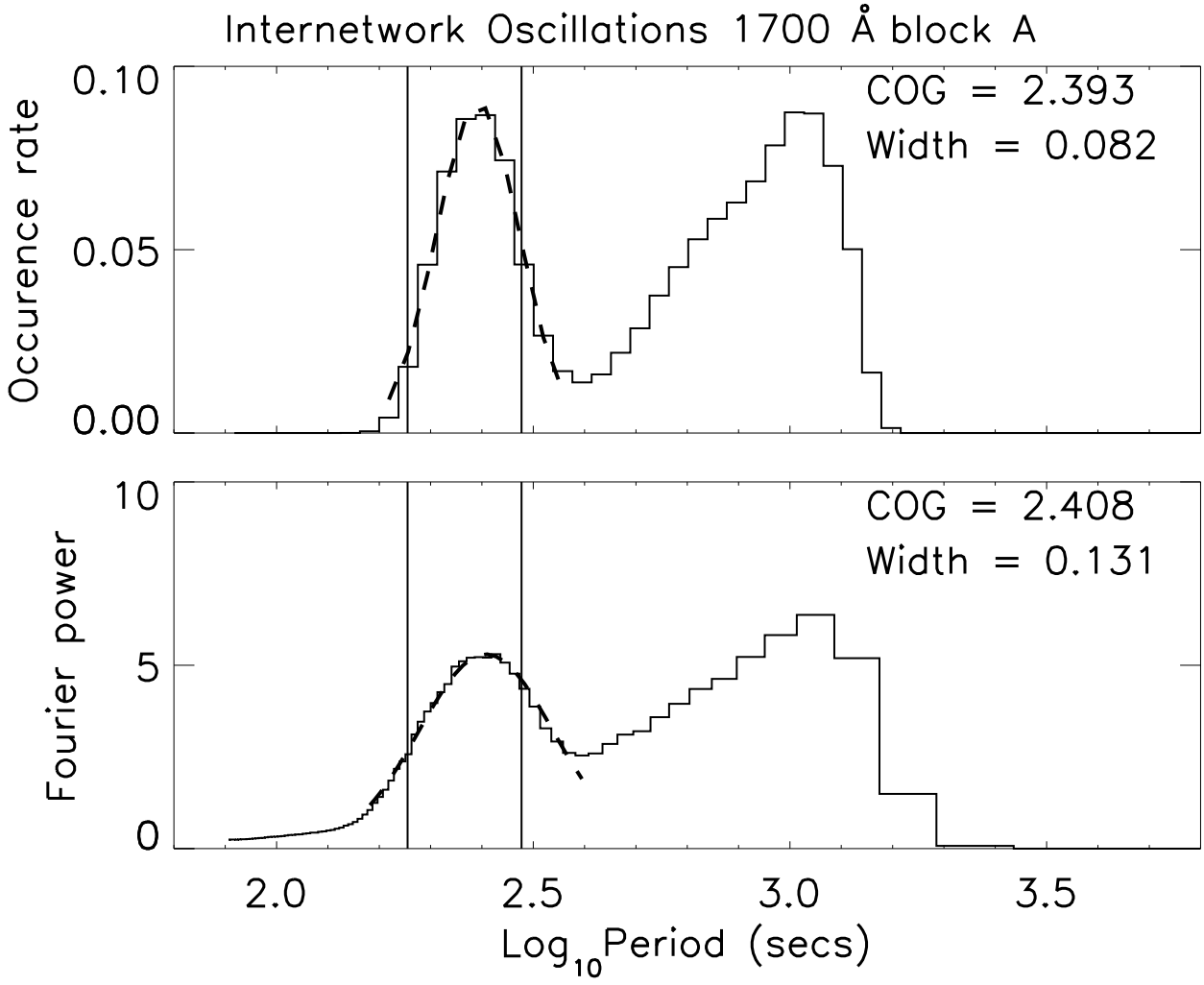

Fig. 4.— Occurrence rate (top) and Fourier power (bottom) per pixel for all internetwork pixels in the 1700 Å block A dataset. In both portions, a Gaussian fit (dashed line) is applied to the feature around $\log_{10}(P)$=2.4, and the centre and one sigma width of this Gaussian fit is displayed at the top right.

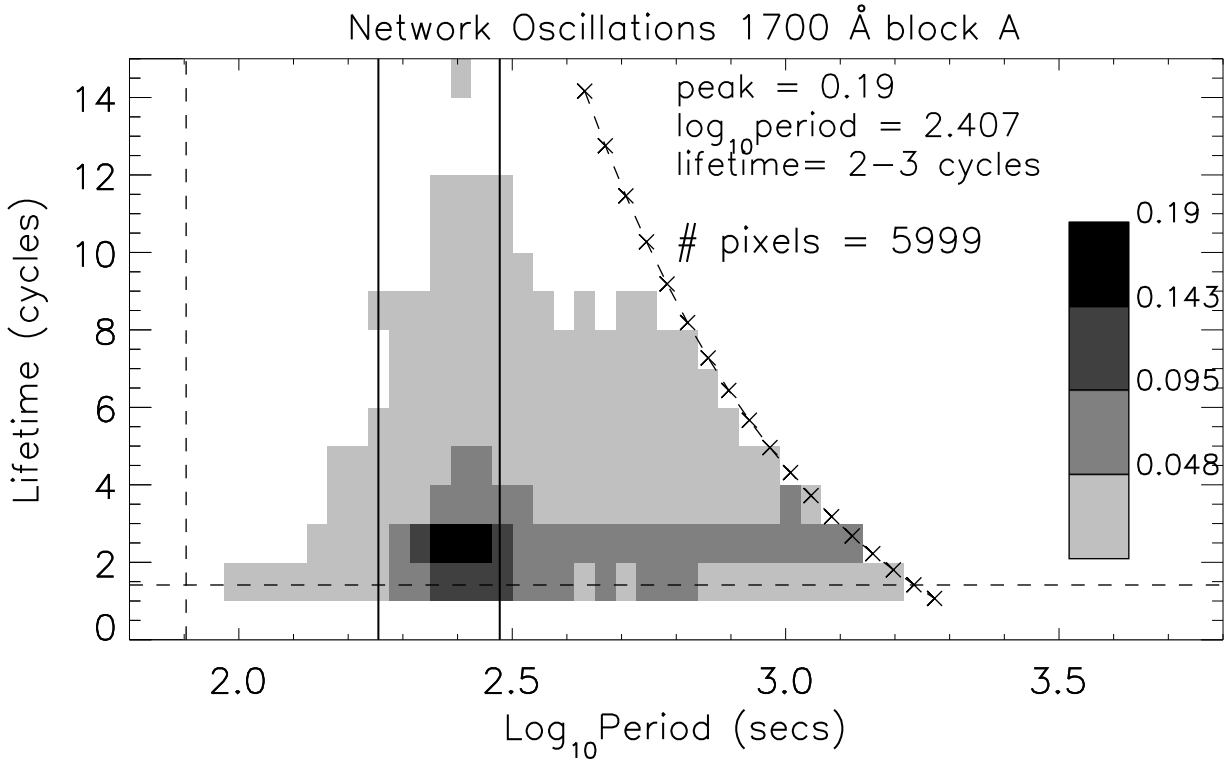

Fig. 5.— Summary of all network oscillations for the 1700 Å block A dataset (5999 pixels). The frequency of occurrence of any oscillation at each period and lifetime is plotted according to the intensity scale on the right. The dashed vertical and horizontal lines are at the Nyquist frequency and minimum lifetime, respectively. The two solid vertical lines are at 3 and 5 min. The curved dashed line defines the maximum detectable number of cycles for each period. The four shades of grey corresponds to >75%, 50–75%, 25–50%, <25% of the maximum value (0.19).

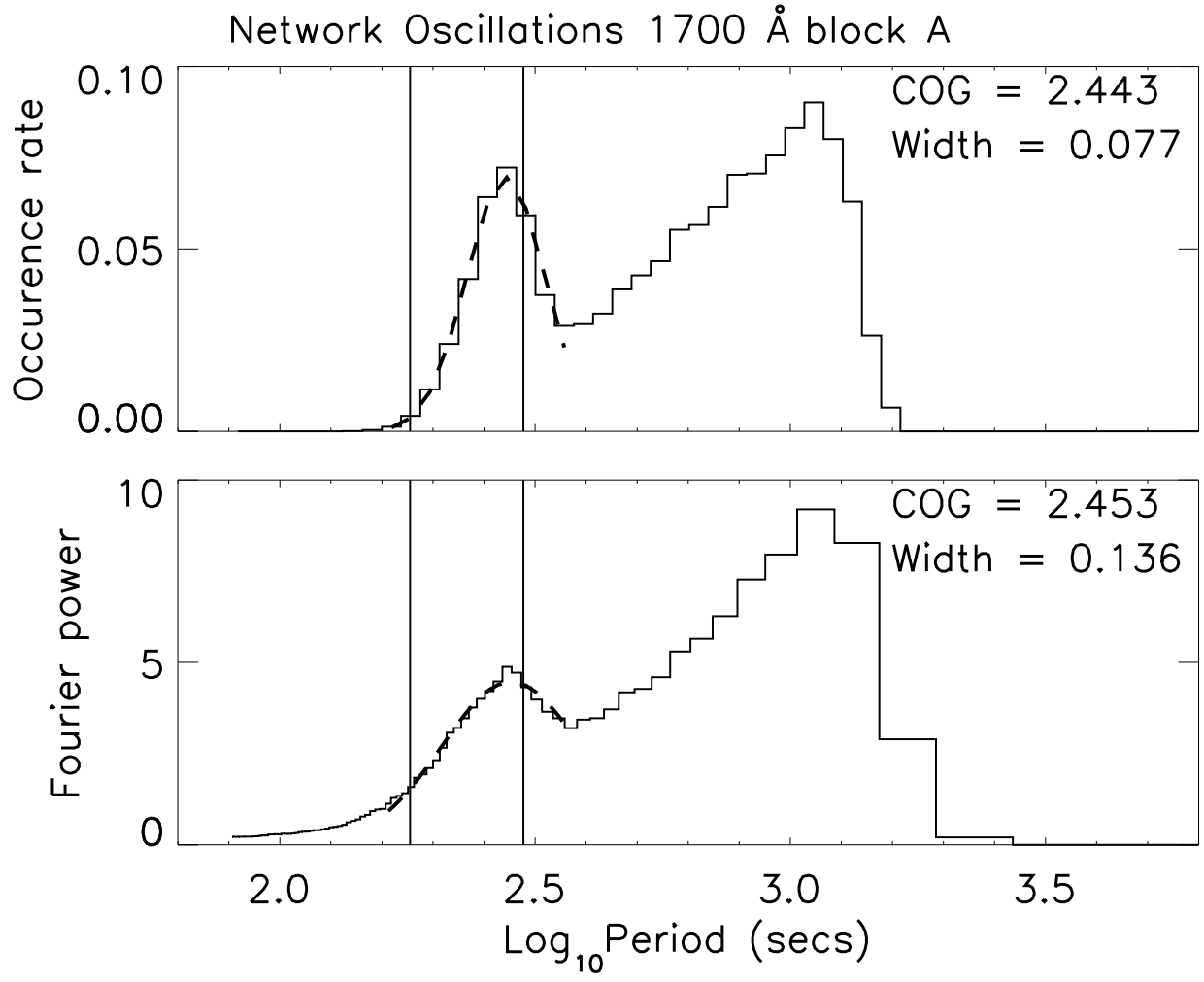

Fig. 6.— Occurrence rate (top) and Fourier power (bottom) per pixel for all network pixels in the 1700 Å block A dataset. In both portions, a Gaussian fit (dashed line) is applied to the feature around $\log_{10}(P)$=2.4, and the centre and one sigma width of this Gaussian fit is displayed at the top right.

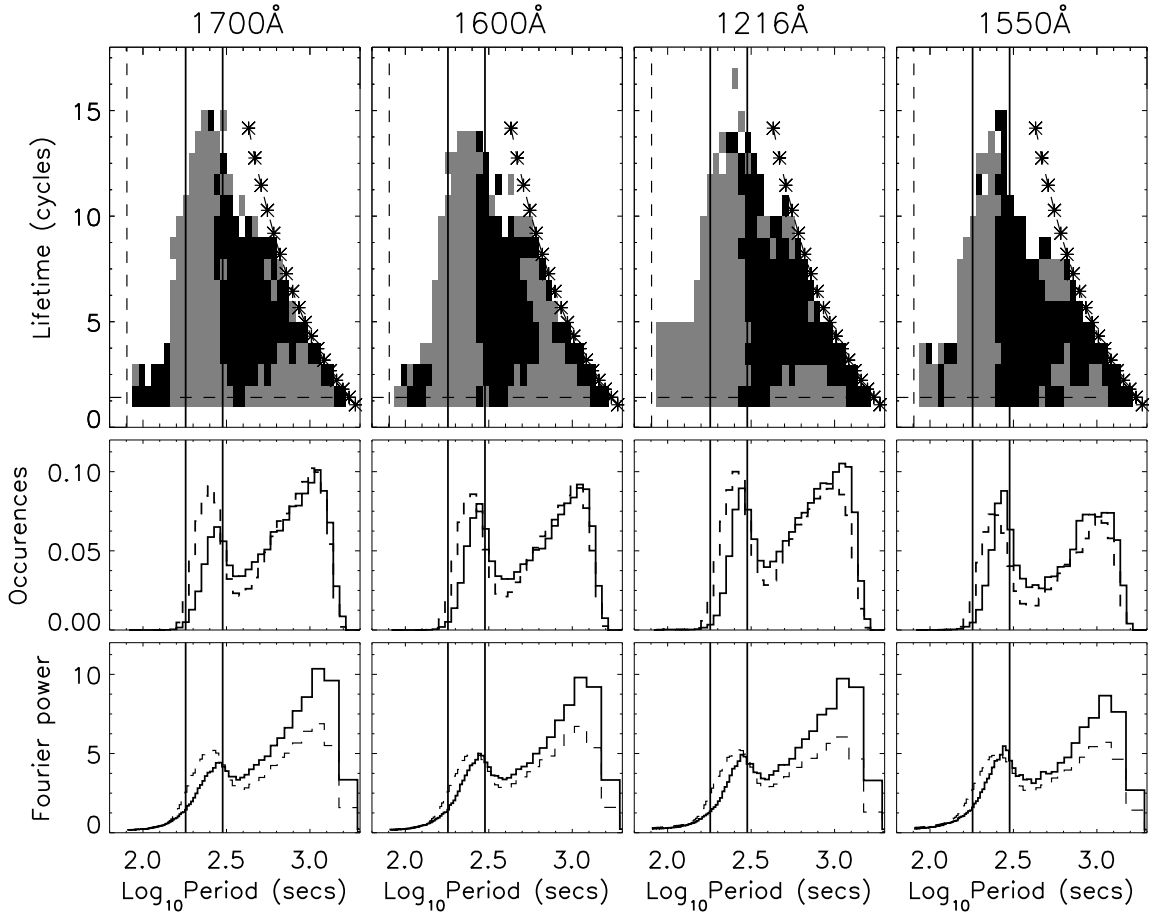

Fig. 7.— Comparison of network and internetwork oscillatory behaviour. Rows: Top - Same axis and lines as Figures 3 and 5. Grey areas are where the internetwork displays more oscillations, black areas are where the network display more oscillations, for each period and lifetime. Middle - Average occurrence rate per pixel at each period for the network (solid) and internetwork (dashed). Bottom - Average Fourier power per pixel at each period for network (solid) and internetwork (dashed). Columns: Increasing height of formation from left to right; 1700 Å, 1600 Å, 1216 Å, 1550 Å

Table 1: Centres and one sigma widths (both in $\log_{10}$ seconds) of the Gaussian fits to the occurrence rate and Fourier power curves for the first half (block A) and second half (block B) in each bandpass.

Wavelength	Network				Internetwork			
Dataset	Wavelet		Fourier		Wavelet		Fourier	
	Centre	Width	Centre	Width	Centre	Width	Centre	Width
1550 A	2.441	0.080	2.460	0.141	2.391	0.089	2.408	0.143
1216 A	2.457	0.084	2.462	0.127	2.413	0.093	2.421	0.136
1600 A	2.440	0.081	2.452	0.135	2.391	0.084	2.407	0.136
1700 A	2.443	0.077	2.453	0.136	2.393	0.082	2.408	0.131
1550 B	2.455	0.089	2.479	0.166	2.401	0.088	2.435	0.166
1216 B	2.464	0.090	2.473	0.136	2.414	0.092	2.421	0.137
1600 B	2.453	0.098	2.470	0.140	2.406	0.096	2.422	0.143
1700 B	2.457	0.100	2.563	0.141	2.409	0.093	2.419	0.137
Average	2.451±0.087		2.464±0.140		2.402±0.090		2.418±0.141	

Table 2: Frequency of occurrence of the most common oscillation (lifetime-period plots), and peak of the Gaussian fit for occurrence rate and Fourier Power of oscillations in the network (NWK) and the internetwork (INWK) for the first half (block A) and second half (block B) in each bandpass. Columns are numbered (2–7) for ease of reference to the text in Section 4.5

	Most Common Osc.		Peak of Gaussian Fit			
Wavelength	Occurrence Rate		Occurrence Rate		Fourier Power	
Dataset	NWK(2)	INWK(3)	NWK(4)	INWK(5)	NWK(6)	INWK(7)
1550 A	0.212	0.229	0.081	0.073	4.80	4.89
1216 A	0.217	0.257	0.086	0.098	4.61	5.12
1600 A	0.206	0.246	0.079	0.085	4.82	5.15
1700 A	0.188	0.260	0.070	0.090	4.47	5.30
1550 B	0.120	0.138	0.043	0.041	4.33	4.24
1216 B	0.197	0.254	0.079	0.099	4.55	5.13
1600 B	0.179	0.241	0.071	0.088	4.48	4.86
1700 B	0.161	0.259	0.058	0.092	3.96	5.02